



Kinetic Particle Simulations of Plasma and Dust Environments at Robotic Construction Sites near the Lunar Terminator

Jianxun Zhao¹; Xiaoming He²; Guirong Yan, M.ASCE³; and Daoru Han⁴

Abstract: This paper presents a kinetic particle simulation campaign of plasma and dust environments related to excavation and construction activities at the lunar terminator regions. The electrostatic field caused by the local plasma environment was resolved by a fully kinetic finite-difference (FD) particle-in-cell (PIC) code. Trajectories of lofted charged dust grains were traced in the obtained electric field as well as lunar gravity. Two surface terrain scenarios, one convex and the other concave, were considered, each with three cases of dust generation locations with respect to the surface feature. Results show that under average solar wind conditions, lofted charged dust grains are generally concentrated within several meters from the surface near the location of origination, but some dust grains can be lofted as high as about 80 m from lunar surface. A slight amount of dust can even reach over 100 m and migrate further due to greater dust charge. Based on these results, preferred locations to perform excavation and construction activities are recommended. DOI: 10.1061/(ASCE)AS.1943-5525.0001489.

© 2022 American Society of Civil Engineers.

Introduction

With renewed interest of exploration and establishment on the Moon, the goal of a sustainable human presence on the lunar surface has been made clearly by the National Aeronautics and Space Administration (NASA) Artemis program. Meanwhile, an increasing demand of deeper understanding of in situ activities on the lunar surface has shown in various fields of studies such as plume—surface interaction during landing and descending (Metzger 2005; Metzger et al. 2008, 2011; Lane et al. 2010; Watkins et al. 2021) and transportation of lunar regolith for construction purposes (Kawamoto 2020). In order to achieve long-term and sustainable presence and explorations on the Moon, in situ resource utilization (ISRU) is considered to be of critical importance as shown in recent literature. Particularly, lunar regolith, which consists of mainly metals, oxygen, and helium 3, is considered as one of the ideal substances to support human activities on the Moon.

For instance, Baiden et al. (2010) discussed the possibility of building a permanent outpost on the Moon and gave suggestions on the construction of such an outpost with current technologies. According to that study, an ideal lunar outpost would be constructed underground to protect astronauts, plants, and animals

Note. This manuscript was submitted on January 2, 2022; approved on June 15, 2022; published online on September 5, 2022. Discussion period open until February 5, 2023; separate discussions must be submitted for individual papers. This paper is part of the *Journal of Aerospace Engineering*, © ASCE, ISSN 0893-1321.

from significant environmental hazards including lunar radiation, temperature extremes, solar flares, and so on. The in situ resources for constructions, i.e., lunar regolith, could be obtained through underground mining on the Moon with automated or teleoperated control from the Earth. The authors concluded that the underground lunar outpost is necessary for long-term human activities and it is feasible to be constructed with existing technologies. More recently, Kawamoto (2020) studied the ISRU with lunar regolith and presented a vibration transport system to transport lunar regolith more efficiently. Metzger et al. (2020) investigated the possibility of obtaining water by thermal extraction of volatiles from lunar or asteroid regolith through computer modeling.

As outlined in the NASA Artemis Plan, habitats or other lunar surface structures near the lunar south pole, which is the destination of the Artemis program, could be built using in situ resources (NASA 2020). Therefore, frequent excavation and construction activities are expected, as mentioned in the literature. For instance, Woodcock et al. (1990) collected studies from NASA's contractor contributors and presented a report of the application of automation and robotics on lunar surface operations. This report broadened the assessment of the operational problems that could be encountered during the process of expanding human presence into the solar system, and provided possible solutions. Gawronska et al. (2020) photogeologically analyzed the geologic features near the lunar south pole in order to target potential extravehicular activities. Austin et al. (2020) presented a study of Robotic Lunar Surface Operations 2 (RLSO2) with contemporary tools (computer-aided design engineering, numerical operations model, and so on), and gave overviews of current understandings of lunar operations in terms of assumption, methodology, and element design.

Unlike most of the excavation and construction activities on Earth, which are subject to Earth's gravity and atmosphere, every simple process on the Moon could encounter a series of issues because of the reduced gravity and lack of a considerable atmosphere, as well as being directly exposed to solar radiation and various space plasma environments that interact with the lunar surface and structures. As a result of such interactions, the lunar surface is electrically charged by the bombardment of solar wind plasma and emission/collection of photoelectrons. Additionally, dust grains on

¹Graduate Research Assistant, Dept. of Mechanical and Aerospace Engineering, Missouri Univ. of Science and Technology, 400 W. 13th St., Rolla, MO 65409.

²Professor, Dept. of Mathematics and Statistics, Missouri Univ. of Science and Technology, 400 W. 12th St., Rolla, MO 65409.

³Associate Professor, Dept. of Civil, Architectural, and Environmental Engineering, Missouri Univ. of Science and Technology, 1401 N. Pine St., Rolla, MO 65409.

⁴Assistant Professor, Dept. of Mechanical and Aerospace Engineering, Missouri Univ. of Science and Technology, 400 W. 13th St., Rolla, MO 65409 (corresponding author). ORCID: https://orcid.org/0000-0001-6186-1777. Email: handao@mst.edu

the lunar surface may get charged and levitated from the surface under the influence of the electric field within the plasma sheath as well as lunar gravity. The interactions between the plasma environment and charging/levitation/transport of dust grains near the lunar surface under natural conditions without human perturbation have been studied extensively (e.g., Fu 1971; Zook and McCoy 1991; Nitter et al. 1998; Abbas et al. 2007; Halekas et al. 2007; Wang et al. 2008, 2016; Poppe et al. 2011, 2012; Zimmerman et al. 2016) and references therein. Recent studies have also been carried out to study surface charging near landers (Anuar 2013) and outposts (Han et al. 2018).

For human lunar explorations and activities, lunar dust has been considered as one of the greatest challenges and studied ever since dust issues were observed during the Apollo missions (Godwin 2002). By collecting and reviewing the reports of Apollo Program, Wagner (2006) described the details of lunar dust issues and recommended that in order to achieve successful lunar surface explorations, the lunar dust effects have to be considered when designing every system that has contact with lunar dust. Recently, attentions have also been paid to effects of lunar dusts on spacesuits (Christoffersen and Lindsay 2009) and astronaut health (Corazzari et al. 2021), as well as mitigation schemes (Farr et al. 2020).

This study focuses on plasma and dust environments related to excavation and construction activities at the lunar polar regions. In these scenarios, dust grains can be charged by solar wind bombardment and photoemission, as mentioned previously, for space environments and recently observed in ground experiments (Carroll et al. 2020), as well as triboelectric charging caused by human activities such as drilling in the shadow region on the lunar surface (Rhodes et al. 2020). The objective is to reveal the complex plasma and dust environments near construction sites and investigate possible issues from the electrostatic and dust perspectives. The work presented here builds upon previous studies carried out on space-craft charging and dust interactions (Wang et al. 2007) and electrostatic dust levitation on a flat lunar surface (Wang et al. 2008) and extends the scenarios to uneven lunar surface terrains with dust levitation caused by surface construction activities.

The rest of this paper is organized as follows. Section "Modeling Approach" describes the modeling approaches for plasma environment and transport dynamics of charged dust grains. Section "Results for Convex Lunar Surface" and section "Results for Concave Lunar Surface" presents results and analysis for convex and concave surface terrains, respectively. Finally, section "Summary and Conclusion" gives a summary and conclusion.

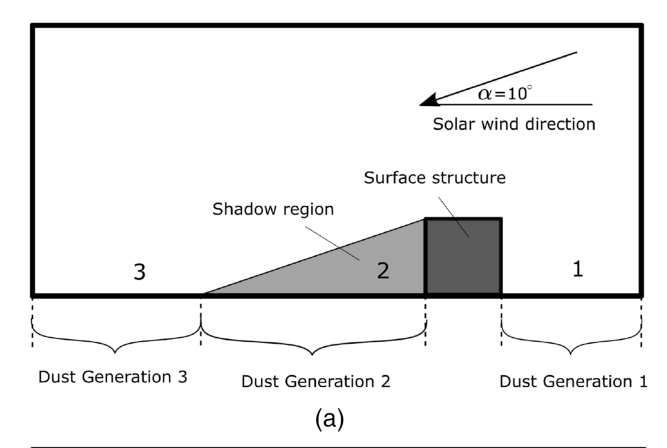
Modeling Approach

Problem Description and Simulation Setup

We consider two representative surface terrains for excavation and construction scenarios at the lunar terminator with latitude of about 80°, i.e., solar wind impinging the lunar surface at a 10° angle of attack. One terrain is convex, representing a surface structure as shown in Fig. 1(a), and the other concave, representing a pit as shown in Fig. 1(b). For each terrain, we consider three locations of dust generation, denoted as Locations 1, 2, and 3 in Fig. 1. The interactions among the local-scale plasma environment, charged dust grains, and lunar surface/structures, are modeled as described next.

Modeling the Plasma Environment

The local plasma environment consists of mainly solar wind ions and electrons, as well as photoelectrons. At the local scale, the plasma sheath formed near the illuminated lunar surface is



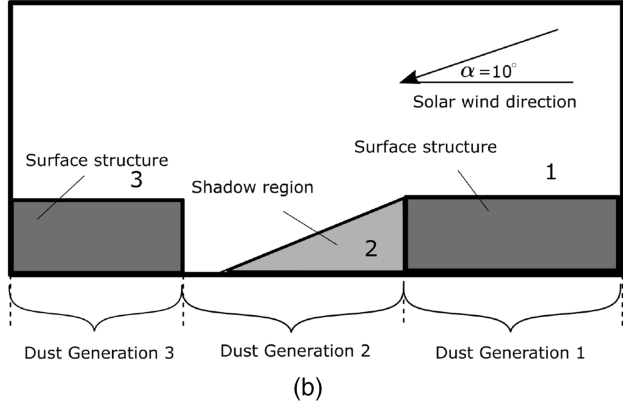


Fig. 1. Problem description: (a) convex terrain representing a surface structure; and (b) concave terrain representing a pit.

dominated by photoelectrons. Therefore, it is usually referred to as the photoelectron sheath (Fu 1971; Nitter et al. 1998; Zhao et al. 2021a). In this work, the plasma environment is solved through a fully-kinetic three-dimensional (3D) finite-difference (FD) particle-in-cell (PIC) code (Wang et al. 2008; Zhao et al. 2020, 2021b) where the electric field and trajectories of charged particles are solved self-consistently through Poisson's equation together with the equations of motion of charged particles.

Plasma Conditions and Normalization

In this study, we considered the plasma species of the average solar wind conditions at 149,598,000 km (1 AU) including solar wind electrons and ions as well as photoelectrons near the lunar surface (Wang et al. 2008; Lund et al. 2020; Zhao et al. 2020). The solar wind was assumed to be traveling to the lunar surface in a straight line with a Sun elevation angle (SEA) of 10° and velocity of 468 km/s. The solar wind electrons and ions were considered as thermal with a temperature of 12 and 10 eV, respectively. The density of both solar wind electrons and ions was 8.7 cm⁻³. The temperature of the photoelectrons was 2.2 eV. The density of photoelectrons on the lunar surface depends on the local SEA. The parameters of solar wind and photoelectrons are listed in Table 1.

In the FD-PIC, plasma parameters in the simulations were normalized by reference values listed in Table 2, where λ_d is the Debye length of a photoelectron at 90° SEA (1.38 m); $T_{\rm phe}$ is the photoelectron temperature (2.2 eV); $m_{\rm phe}$ is the mass of a photoelectron; k is the Boltzmann constant; e is electric charge; $v_{\rm phe,\it f} = \sqrt{kT_{\rm phe}/m_{\rm phe}}$ is the thermal velocity of photoelectrons as a velocity reference; and $n_{\rm phe,ref}$ is the photoelectron number density at 90° SEA. The physical time was normalized by $1/\omega_{\rm phe}$, where $\omega_{\rm phe}$ is the plasma frequency of the photoelectron at normal incidence condition (90°).

Previous work studied the plasma structure of a one-dimensional (1D) photoelectron sheath near flat or uneven lunar surfaces (Zhao et al. 2020, 2021a, b). In this study, we extend the scenarios to two-dimensional (2D) surface terrains with transport dynamics of charged dust grains where the solar wind electrons and ions travel into the computation domain through the X-Z plane (Figs. 2–4).

Table 1. Solar wind and photoelectron parameters

Species	Solar wind electrons	Solar wind ions	Photoelectrons
Drifting velocity (km/s)	468	468	_
Density (cm ⁻³)	8.7	8.7	64 $\sin(\alpha)$
Temperature (eV)	12	10	2.2
Sun elevation angle (degrees)	10	10	10

Note: α = Sun elevation angle.

Table 2. Normalization references in FD-PIC

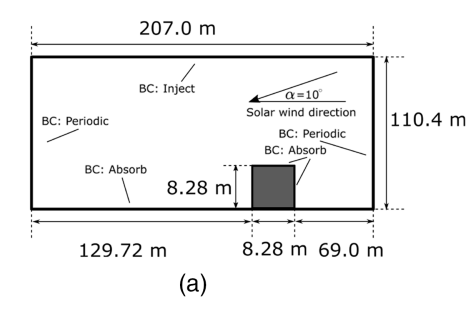
Reference quantities	Parameters used as references	
L_{ref}	λ_d	
$T_{\rm ref}$	$T_{ m phe}$	
m_{ref}	$m_{ m phe}$	
$\phi_{ m ref}$	$kT_{ m phe}/e \ v_{ m phe,t} \ n_{ m phe,ref}$	
$v_{ m ref}$	$v_{\mathrm{phe},t}$	
n_{ref}	$n_{ m phe,ref}$	
$t_{\rm ref}$	$1/\omega_{ m phe}$	

Computation Domain and Boundary Conditions

Computation Domain and Mesh. The dimension of the computation domain for both cases was set as $150 \times 2 \times 80$ total PIC cells (physical dimension of $207.0 \times 2.76 \times 110.4$ m), as shown in Fig. 2. For the convex surface, a structure with a dimension of $6 \times 2 \times 6$ PIC cells (physical dimension of $8.28 \times 2.76 \times 8.28$ m) representing a lunar surface structure is located on a flat surface with a shadow region behind, as shown in Fig. 3(b). Whereas for the concave surface, a rectangular pit with a dimension of $50 \times 2 \times 6$ PIC cells (physical dimension of $69.0 \times 2.76 \times 8.28$ m) is located in the center of the computation domain (depth of 8.22 m), as shown in Fig. 4(b).

Particle Boundary Conditions. For both cases, the particle boundary conditions along *x*- and *y*-directions were set as periodic, which means once a particle travels across the boundary, it enters the computation domain from the opposite boundary with the same properties; thus, the computation domain is able to represent a relatively large area with low computation cost. The bottom surface (lunar surface and structure surfaces) was set as absorb, which means once a particle hits these surfaces, the particle gets absorbed and the charge will be accumulated on the surface. The top surface of computation domain was set as ambient inject, from where the solar wind plasma enters the computation domain. These particle boundary conditions are summarized in Table 3.

Field Boundary Conditions. Zero-Dirichlet boundary conditions of $\phi=0$ were applied for the $Z_{\rm max}$ boundary, which was considered as far field in the numerical simulation. The remaining boundaries were all applied with the zero-Neumann boundary condition with $\partial \phi/\partial n=0$.



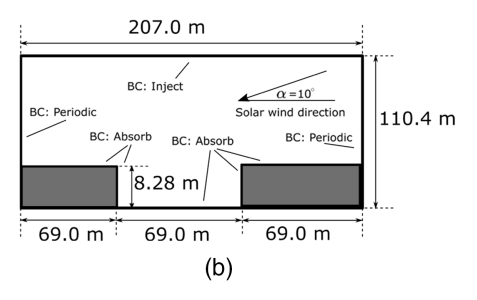


Fig. 2. Computation domains: (a) convex terrain; and (b) concave terrain.

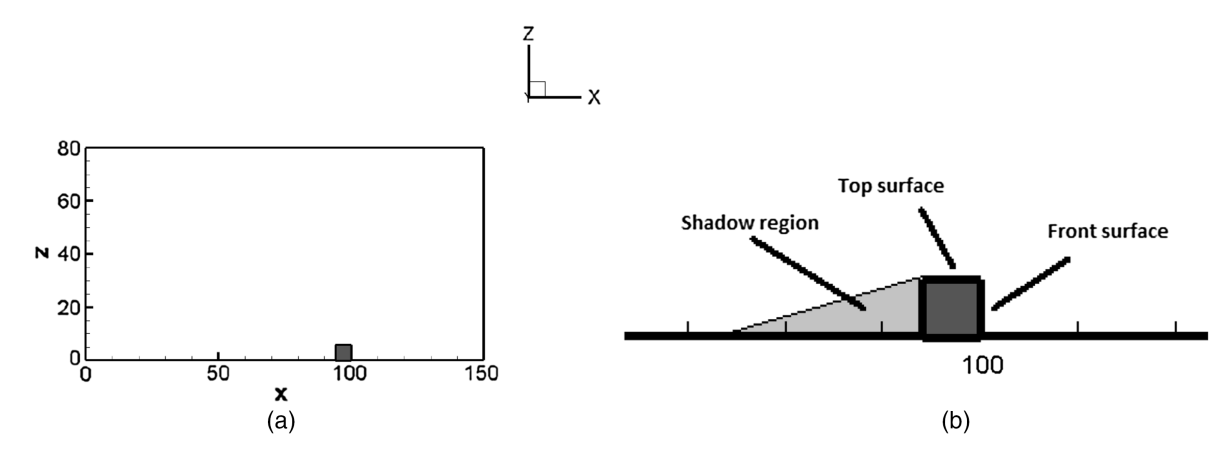


Fig. 3. Convex terrain: (a) computation domain; and (b) zoom-in near the surface structure.

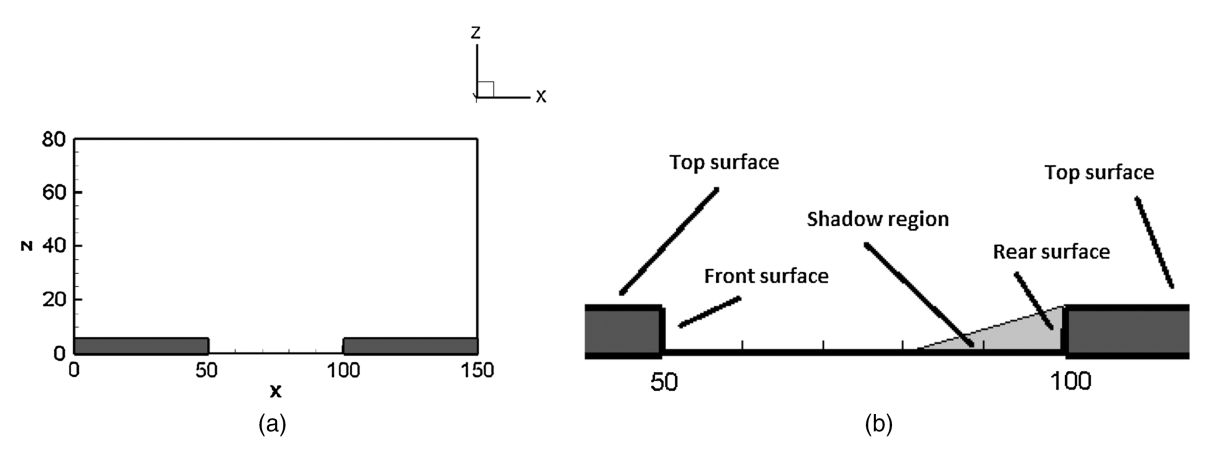


Fig. 4. Concave terrain: (a) computation domain; and (b) zoom-in near the pit.

Table 3. Boundary conditions of PIC simulations

Boundary condition location	Boundary condition type
BC along x	Periodic
BC along y	Periodic
Bottom BC	Absorb
Top BC	Ambient inject

Note: BC = boundary condition.

For each FD-PIC simulation, 3,600,000 simulation particles representing solar wind electrons and ions (1,800,000 for each species) were preloaded into the computation domain at the beginning of the simulation. Within each PIC time step, another \sim 12,000 simulation particles representing solar wind electrons and ions (\sim 6,000 for each species) and \sim 7,500 simulation particles representing photoelectrons were injected into the computation domain according to boundary conditions. The simulations ran 100,000 steps for each case, which is \sim 900 s in physical units. The wall clock time was \sim 10 h for each FD-PIC run.

Modeling Charged Dust Transport

We consider the transport of charged dust grains originated from different initial locations on lunar surface (Fig. 1). All dust grains were assumed as spherical particles with radius r_d . The lunar dust density was chosen as $\rho_d \approx 2.65~{\rm g/cm^3}$, which is the density of lunar soil (Heiken et al. 1991). The gravitational acceleration on the Moon is $g=1.67~{\rm m/s^2}$. Because the time scales of plasma dynamics and dust transport are quite different due to very different masses, in this study, the charged dust grains were traced in a frozen electrostatic field established by the plasma species at the steady state.

Generation of Lofted Charged Dust Grains

The electrostatic levitation of charged lunar dust grains will occur when enough charge accumulates on the dust and the corresponding upward electrostatic force acting on the dust becomes greater than the gravity. The dust can also be levitated by disturbance of human or mechanical activities, such as robotic construction. In this study, three dust levitation locations were considered, and they are illustrated as Cases 1, 2, and 3 in Fig. 1. For the convex surface, dust grains in Case 1 are generated from the lunar surface in front of the structure (upwind of the solar wind). In Case 2, dust grains are originated inside the shadow region behind the structure (downwind of the solar wind). Whereas in Case 3, dust grains are

generated outside the shadow region behind the structure. For the concave surface, in Case 1 the dust grains are generated on the surface in front of the pit, in Case 2 the dust are originated from the bottom surface of the pit. In Case 2, the dust grains are generated along the entire bottom surface ($\hat{x} = 50-100$), whereas the shadow region only covers ~3/4 of the bottom surface, as shown in Fig. 1(b). In Case 3, the dust grains are generated on the surface behind the pit.

As mentioned previously, all dust grains were considered as spherical particles with radius r_d . In this study, we considered two dust sizes, one of $r_d = 1.0 \times 10^{-6}$ m and the other $r_d = 10.0 \times 10^{-6}$ m. To compare the effects of dust sizes on dust transport, all other parameters were kept the same in the simulations. The initial number density of lofted dust grains near the lunar surface was estimated as follows. In natural conditions, number density of dust grains near the lunar surface has been found to be as low as 10^{-4} to 10^{-1} cm⁻³ (McCoy and Criswell 1974; Gault et al. 1963; Hartung et al. 1972; Sharma et al. 2021). In the presence of human activities, the number density of levitated dust can be significantly higher.

Morris et al. (2016) studied the dust transport caused by engine plume impingement and presented that the dust number density within a 10-m height from lunar surface ranged from 1.0×10^{-1} to 2.0×10^2 cm⁻³, caused by the plume of one engine hovering at 3 to 20 m from the lunar surface. For construction activities, we estimated the number density of levitated dust to be lower than that caused by engine plumes, i.e., less than or on the same order of magnitude of the ambient solar wind (~10 cm⁻³). In this study, we normalized the initial number density of the lofted dust to be 1.0 and present normalized dust number densities for each case.

Transport of Charged Dust Grains

Once a dust grain is levitated, the motion of the dust will be determined by the surrounding electric field and lunar gravity. In the simulations, the charged dust grains were assumed to be levitated from the lunar surface with a small upward velocity (caused by electrostatic levitation and/or triboelectric charging). The transport of a charged dust grain follows Newton's second law as shown in Eq. (1)

$$\mathbf{F} = m_d \frac{\mathrm{d}\mathbf{v}}{\mathrm{d}t} = Q_d \mathbf{E}(\mathbf{x}) - m_d g \tag{1}$$

where m_d and Q_d = mass and charge of the dust grain, respectively; \mathbf{v} and \mathbf{x} = velocity and position vector, respectively; \mathbf{E} = electric field vector, which is obtained from the FD-PIC simulation; and g = lunar

gravitational acceleration. The last term on the right-hand side of Eq. (1), $m_d g$, only applies for the z-direction.

A dust charge model introduced by Wang et al. (2008) was utilized to calculate Q_d , shown in Eq. (2). With this charge model, the charge accumulated on each dust grain was assumed to be large enough to activate the electrostatic levitation; hence, all dust grains were guaranteed to be aloft

$$Q_d = (1 + \delta)Q_{d,\min} \tag{2}$$

where $Q_{d,\min}=(m_dg)/E_s$, where E_s is the electric field along z-axis on the lunar surface [i.e., $E_s=E_z(z=0)$]; and $\delta\ll 1$ gives an initial acceleration to dust grains ($\delta=0.05$ was assumed in this study). The constant value of δ was used to ensure the upward electric force acting on the dust was greater (and only slightly greater) than the downward gravitational force; therefore, these lofted dust grains would stay longer in the computation (instead of falling back to ground shortly after being lofted). Also, because the electric field was calculated through the plasma simulation, depending on the sign (direction) of the local E_s at the lunar surface, the sign of dust charge can be positive or negative.

With the force acting on the dust grains [obtained by Eq. (1)] and the charge accumulated on each dust grain [obtained by Eq. (2)], the governing equations of the motion of dust grains can be obtained as given in Eq. (3) (Wang et al. 2008):

$$\frac{\mathrm{d}^2 x}{\mathrm{d}t^2} = \left[(1+\delta) \frac{E_x(x,z)}{E_s} \right] g$$

$$\frac{\mathrm{d}^2 z}{\mathrm{d}t^2} = \left[(1+\delta) \frac{E_z(x,z)}{E_s} - 1 \right] g \tag{3}$$

where E_x and E_z = electric field along x- and z-directions, respectively.

The process of calculating the concentration of lofted dust, starting from the calculation of plasma and electrostatic environment with FD-PIC, is illustrated in Fig. 5.

Results for Convex Lunar Surface

Plasma Environment

The details of 1D and 2D photoelectron sheath structures have been studied and presented in previous studies (Zhao et al. 2021a, b). Here, we briefly describe the plasma environment for each of the 2D scenarios. Fig. 6 shows the contours of spatial charge densities, electric potential, and vertical electric field for the convex surface.

A nearly neutral potential profile can be observed in most areas above the surface, due to charge neutrality in these areas [Fig. 6(d)]. The emission of photoelectrons from the structure and lunar surface caused by the exposure to sunlight leads to a positive potential on the front and top surfaces of the structure and the lunar surface outside the shadow region. In contrast, the lack of exposure of sunlight leads to a negative potential on the rear surface of the structure, and the lunar surface inside the shadow region. It is reasonable that the potential is much higher near the front surface of the structure due to the larger photoelectron density (caused by the relatively greater incidence angle of sunlight on the front surface) and correspondingly more positive charges accumulated on this surface.

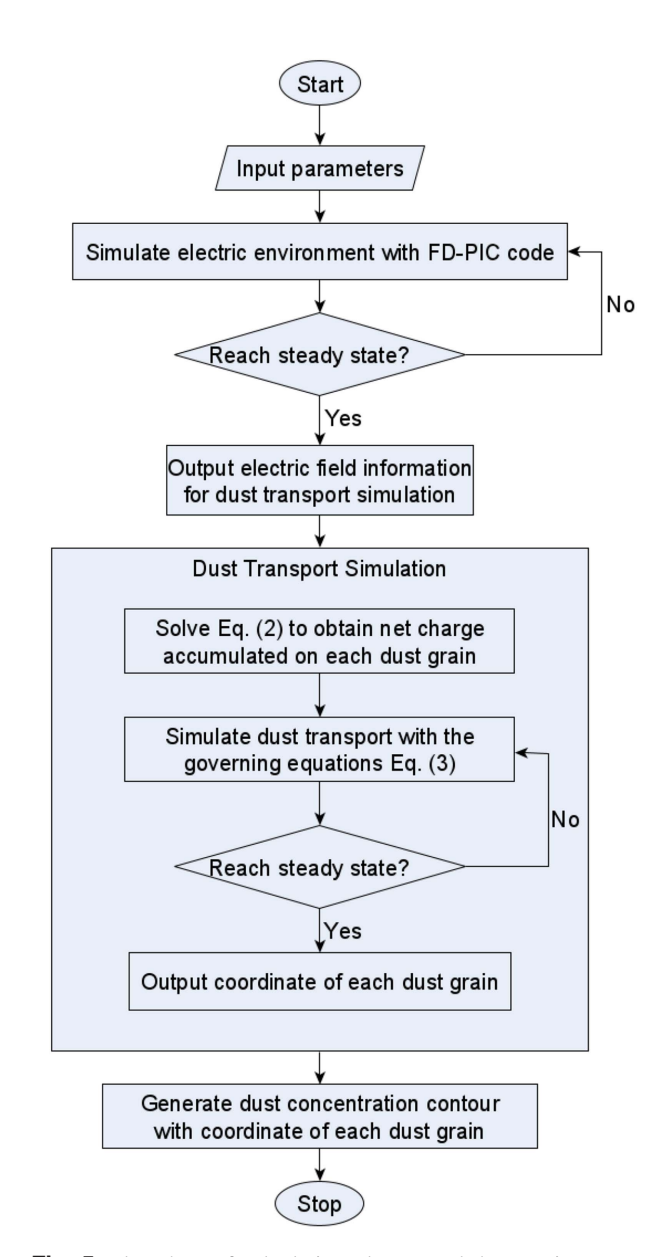


Fig. 5. Flowchart of calculating plasma and dust environments.

Dust Environment

Once the electric field is calculated from the FD-PIC simulations, the motion of lofted charged dust can be calculated with the governing equations introduced in the section "Modeling Charged Dust Transport." The concentration of dust in each case of the two surface terrains are presented subsequently. The dust concentration is a relative value with respect to the concentration of dust initially generated at the surface, i.e., normalized.

Case 1

Fig. 7 shows the dust concentration of Case 1 for two radii ($r_d = 1.0 \times 10^{-6} \, \text{m}$ and $r_d = 10.0 \times 10^{-6} \, \text{m}$). Both radii showed similar trajectories and concentration, indicating that the dust trajectories obtained by this charge model are not affected by dust radius.

According to Eq. (2), the electric charge accumulated on each dust grain (and the corresponding electrostatic force) is linearly proportional to the gravitational force acting on the grain; thus, the motion of lofted dust grains is only controlled by the ambient electric field, which is also true for Case 2 and Case 3. Most of the

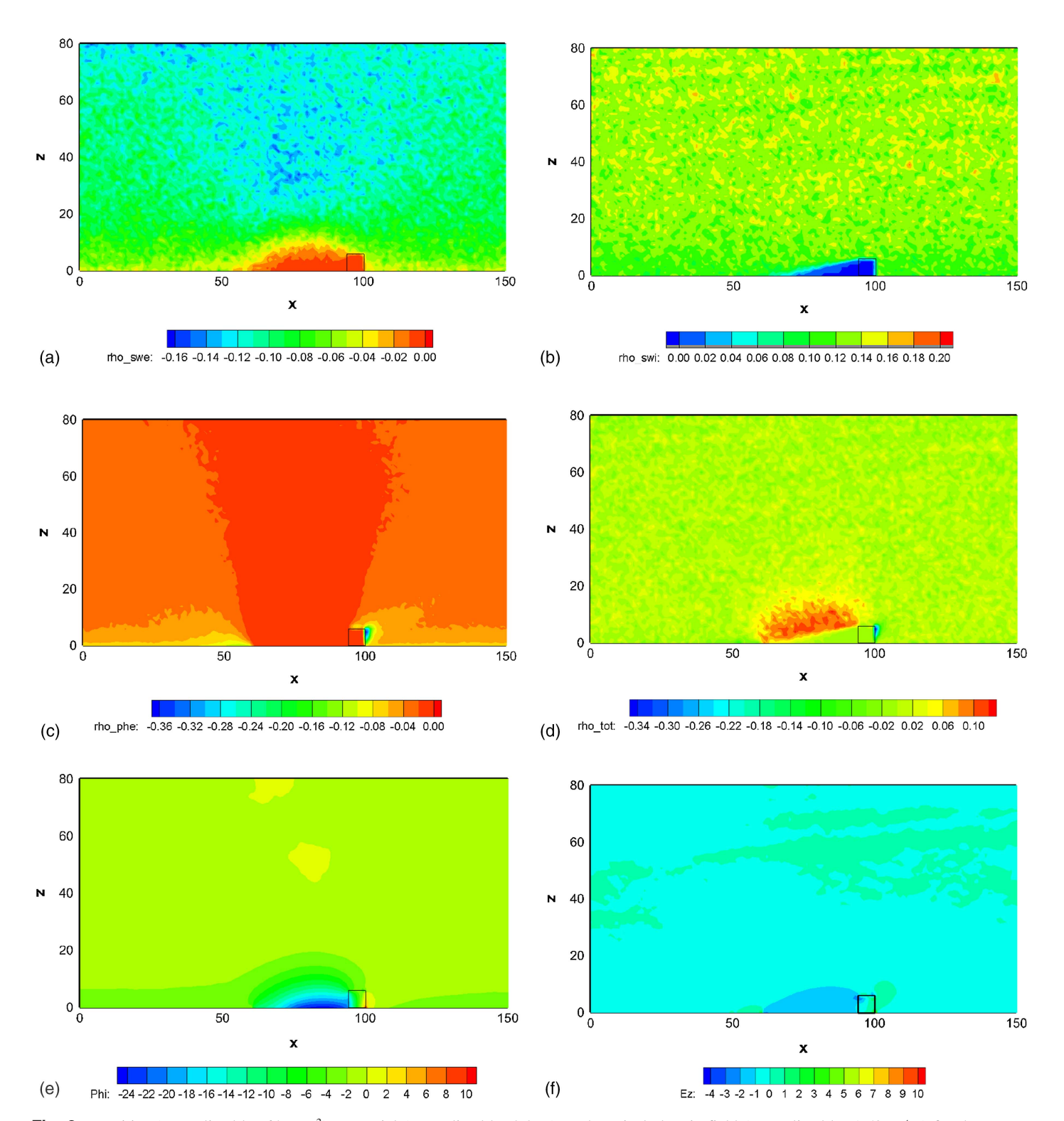


Fig. 6. Densities (normalized by 64 cm^{-3}), potential (normalized by 2.2 V), and vertical electric field (normalized by 1.59 V/m) for the convex surface scenario: (a) solar wind electron density; (b) solar wind ion densit; (c) photoelectron density; (d) total density; (e) potential; and (f) electric field. Electron densities include a negative sign for the negative charge. Coordinates are normalized by 1.38 m.

lofted dusts concentrate within a region of $\sim \! 10$ m above the surface. Some dusts can be lofted to as high as $\sim \! 83$ m. A slight amount of dusts can reach over 100 m and transport further (almost the entire computation domain), which can be caused by the greater accumulated charge on these dusts. However, the lofted dust originated from upwind side (with respect to the solar wind) of the structure are not likely to reach the downwind side of the structure.

Case 2

Fig. 8 shows the dust concentration of Case 2, where the lofted charged dusts originated from the shadow region. Most of the dust will concentrate inside the shadow region with a height of ~20 m. A slight amount of dust can transport further due to the greater initial accumulated charge on these dusts. Similar to Case 1, these dusts are not likely to reach the upwind side of the structure.

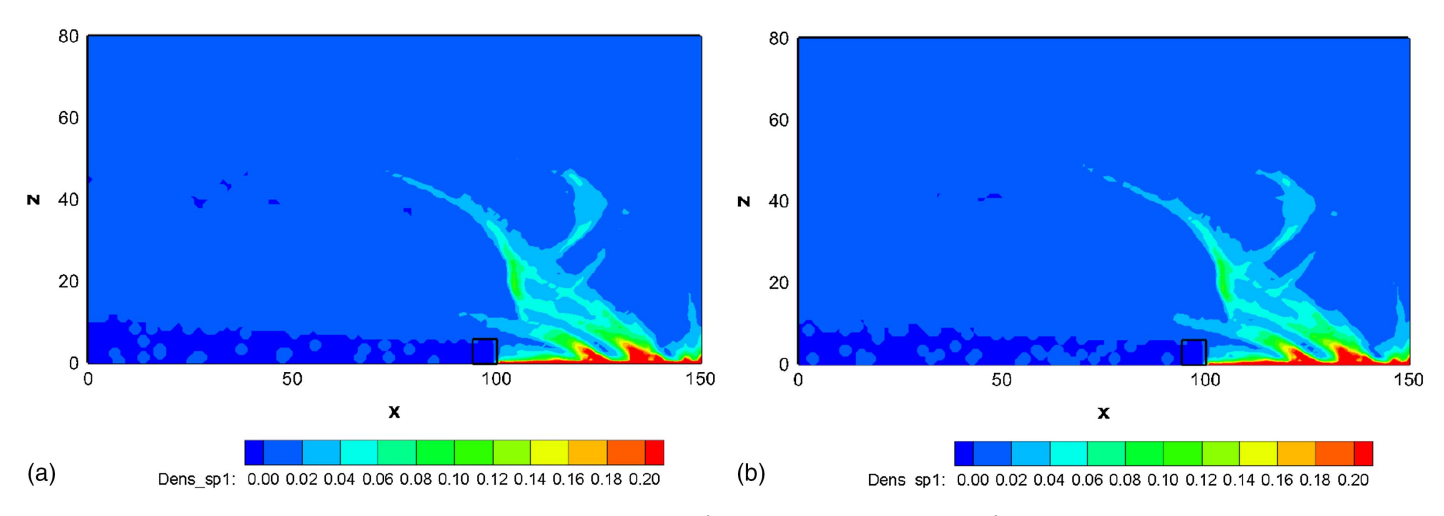


Fig. 7. Normalized dust concentration of Case 1: (a) $r_d = 1.0 \times 10^{-6}$ m; and (b) $r_d = 10.0 \times 10^{-6}$ m. Coordinates are normalized by 1.38 m.

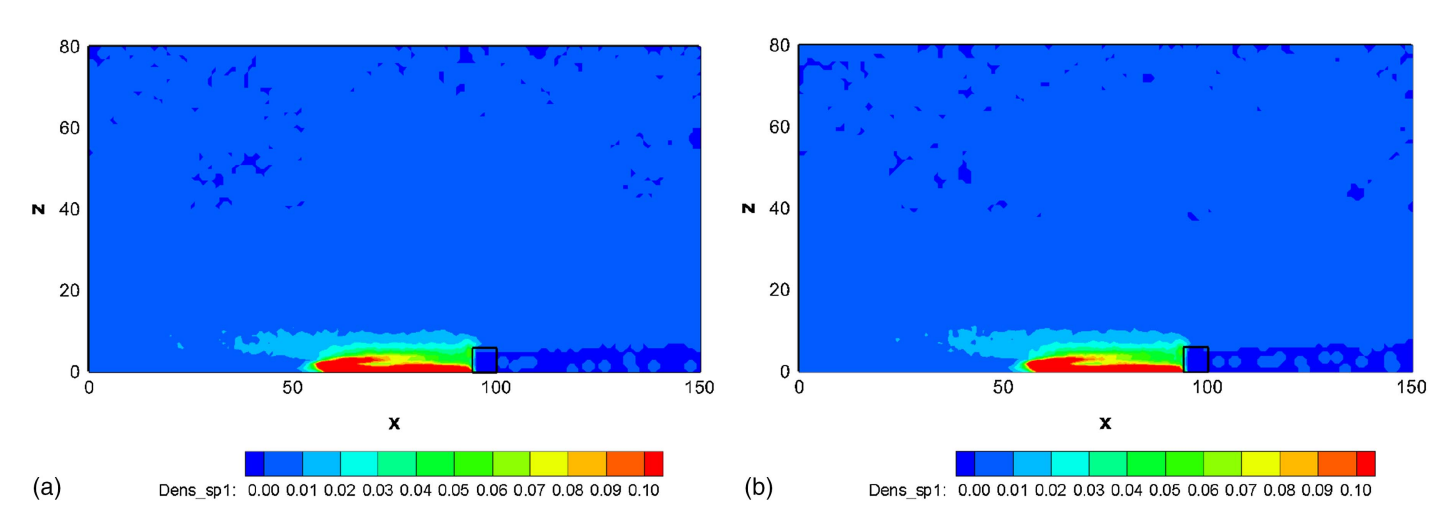


Fig. 8. Normalized dust concentration of Case 2: (a) $r_d = 1.0 \times 10^{-6}$ m; and (b) $r_d = 10.0 \times 10^{-6}$ m. Coordinates are normalized by 1.38 m.

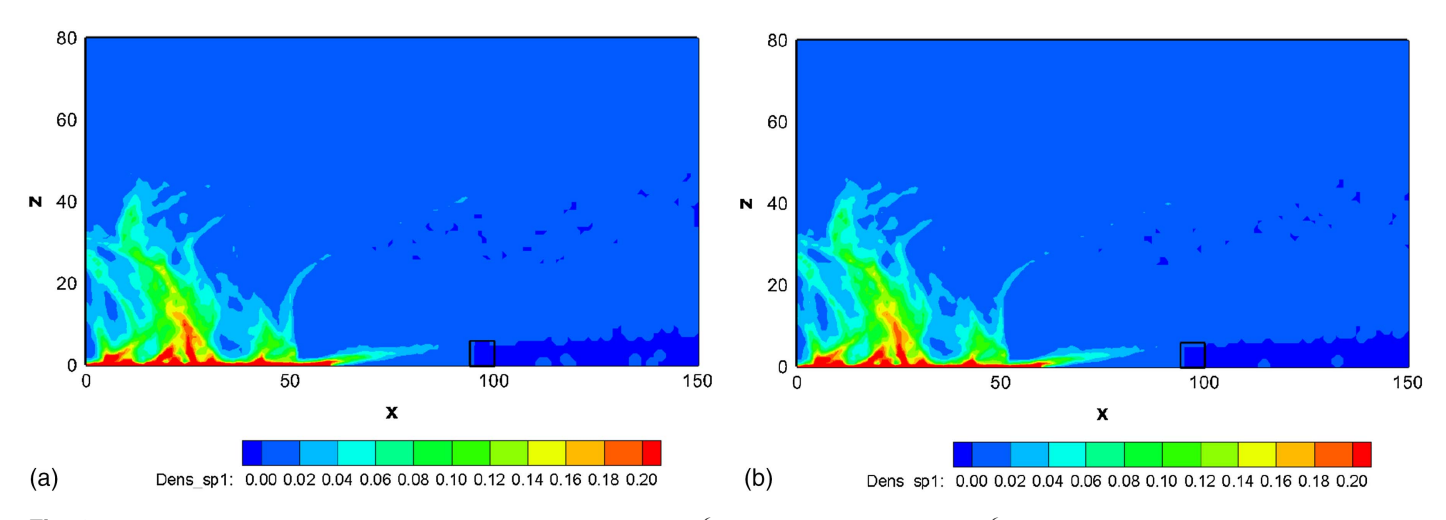


Fig. 9. Normalized dust concentration of Case 3: (a) $r_d = 1.0 \times 10^{-6}$ m; and (b) $r_d = 10.0 \times 10^{-6}$ m. Coordinates are normalized by 1.38 m.

Case 3 Fig. 9 shows the dust concentration of Case 3, where the lofted dusts originated downstream of the shadow region of the structure. Most of the dust will also concentrate below ~10 m height. Some

of the dust can be lofted to as high as ~83 m, which is about the same height in Case 1. Again, a slight amount of dust can transport further, because of the greater accumulated charge. Almost no dust can reach the upwind side of the structure, as shown in Fig. 9.

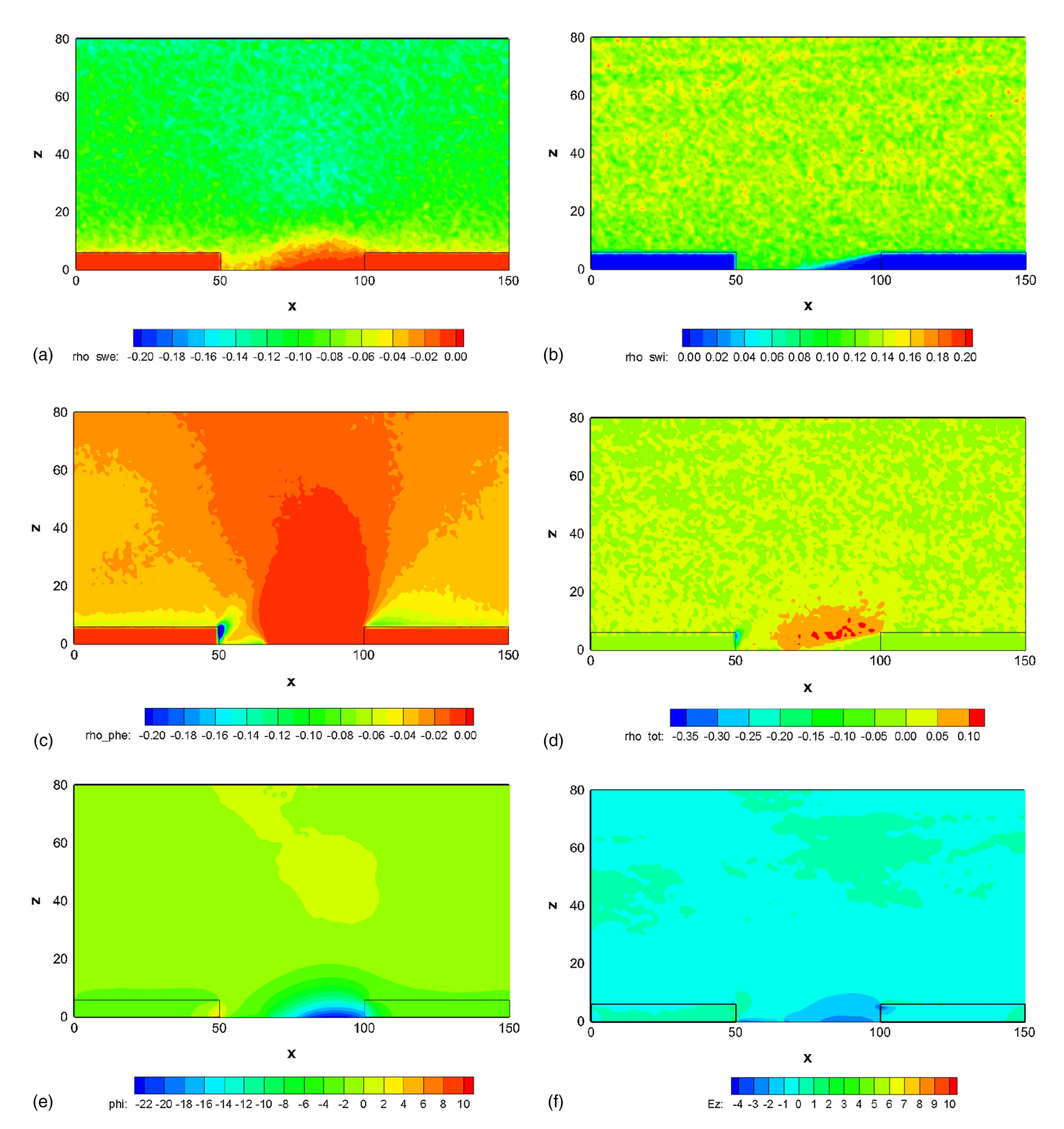


Fig. 10. Densities (normalized by 64 cm⁻³), potential (normalized by 2.2 V), and vertical electric field (normalized by 1.59 V/m) for the concave surface scenario: (a) solar wind electron density; (b) solar wind ion density; (c) photoelectron density; (d) total density; (e) potential; and (f) electric field. Electron densities include a negative sign for the negative charge. Coordinates are normalized by 1.38 m.

Results for Concave Lunar Surface

Plasma Environment

Fig. 10 shows the contours of spatial charge densities, electric potential, and vertical electric field for the concave surface. Similar to the convex scenario, the potential profile is nearly neutral in most

areas above the surface due to the neutrality of the total charge [Fig. 10(d)].

The magnitude of electric potential inside the pit depends on the size of the shadow region. In this specific case, the shadow region only covers part of the surface inside the pit [Fig. 4(b)], hence the potential of the surface outside the shadow region (but still inside the pit) is several volts negative, whereas the potential inside the

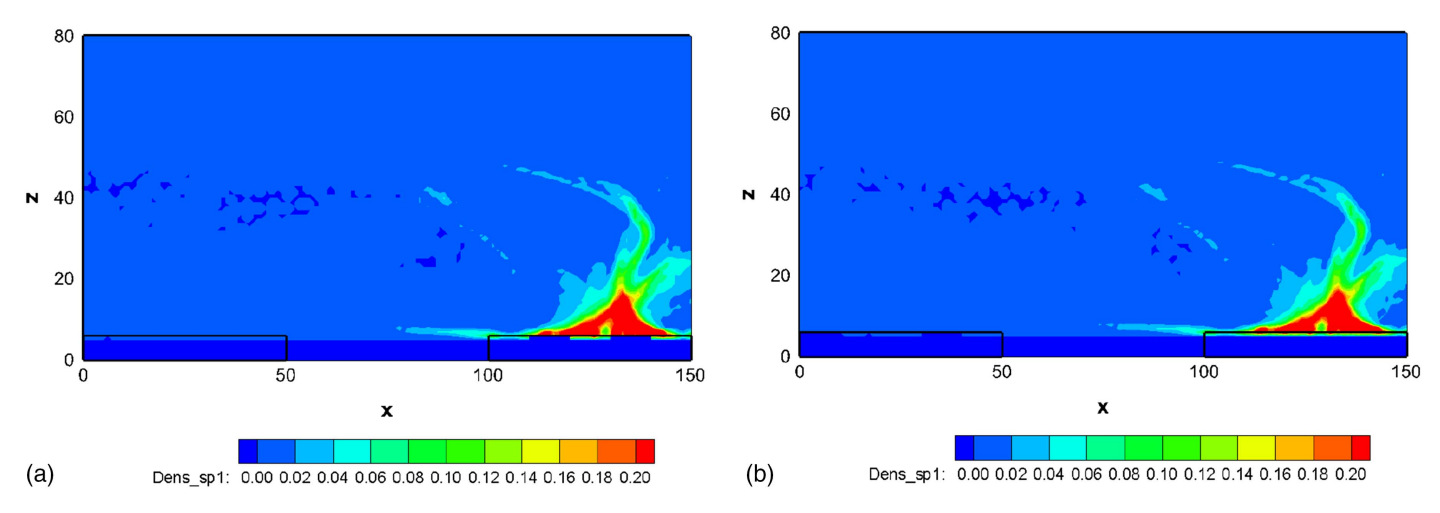


Fig. 11. Normalized dust concentration of Case 1: (a) $r_d = 1.0 \times 10^{-6}$ m; and (b) $r_d = 10.0 \times 10^{-6}$ m. Coordinates are normalized by 1.38 m.

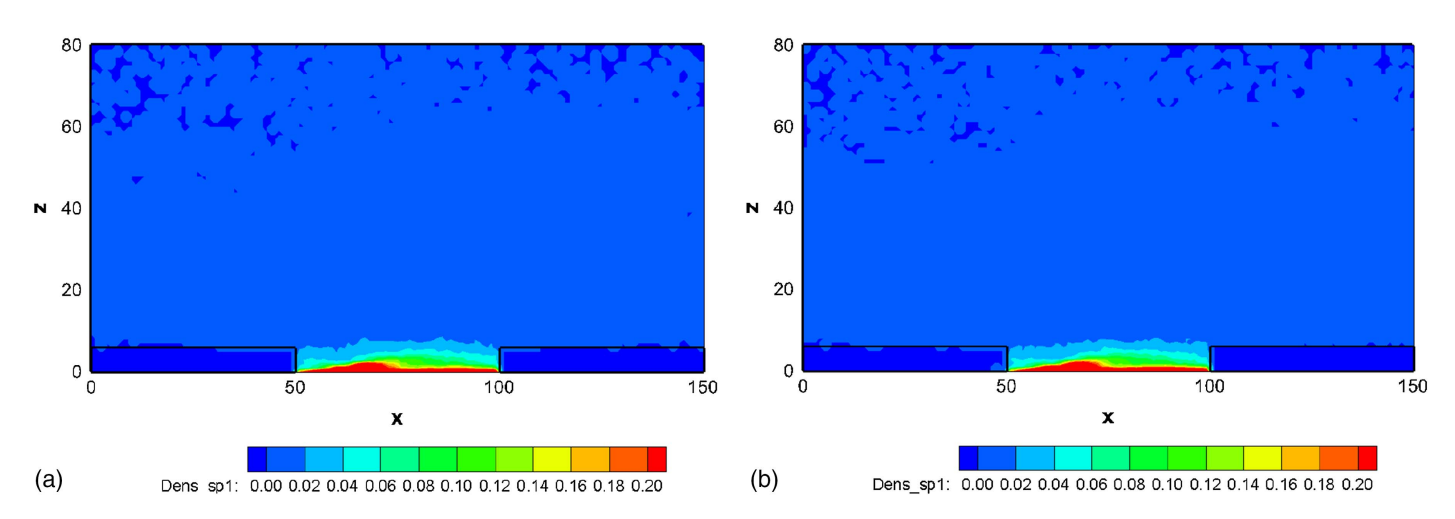


Fig. 12. Normalized dust concentration of Case 2: (a) $r_d = 1.0 \times 10^{-6}$ m; and (b) $r_d = 10.0 \times 10^{-6}$ m. Coordinates are normalized by 1.38 m.

shadow region is more negative with a magnitude of tens of volts due to the collection of highly mobile solar wind electrons and lack of the accumulation of positive charges due to solar wind ions or photoemission [Fig. 10(e)].

Dust Environment

Case 1

Fig. 11 shows the dust concentration of Case 1. Similar to the convex scenario, the lofted charged dust originated in front of the pit will concentrate within $\sim\!20$ m height above the surface ($\sim\!30$ m from the bottom surface inside the pit). Some dust can be lofted to as high as $\sim\!73$ m ($\sim\!83$ m from the bottom surface inside the pit). A slight amount of dust can transport to the entire computation domain due to the greater accumulated charge on these dust. However, almost no dust can transport into the pit.

Case 2

Fig. 12 shows the dust concentration of Case 2, where the lofted charged dusts originated in the shadow region inside the pit. Most of the charged dust will concentrate within the shadow region inside the pit. A slight amount of the dust with greater accumulated charge can transport further (almost the entire computation domain).

Case 3

Fig. 13 shows the dust concentration of Case 3, where the lofted charged dust originated downstream of the pit. Most of the dust will concentrate within \sim 20 m from the surface (\sim 30 m from the bottom surface of the pit). Some dust can be lofted to as high as \sim 70 m (\sim 80 m from the bottom surface of the pit). A slight amount of the charged dust can transport further to the entire computation domain due to the greater accumulated charge. Almost no charged dust can transport into the pit.

Summary and Conclusion

In this study, we investigated plasma and dust environments related to excavation and construction activities at the lunar polar regions through kinetic particle simulations. Particularly, the electrostatic field caused by local plasma environment was resolved by fully kinetic particle-in-cell simulations, and trajectories of lofted charged dust grains were then traced in the obtained electric field as well as lunar gravity. Two surface terrain scenarios, one convex and the other concave, were studied. For each scenario, three cases of dust generation locations were considered. Results showed that under average solar wind conditions, lofted charged dust grains were generally confined near their places of origination. For the

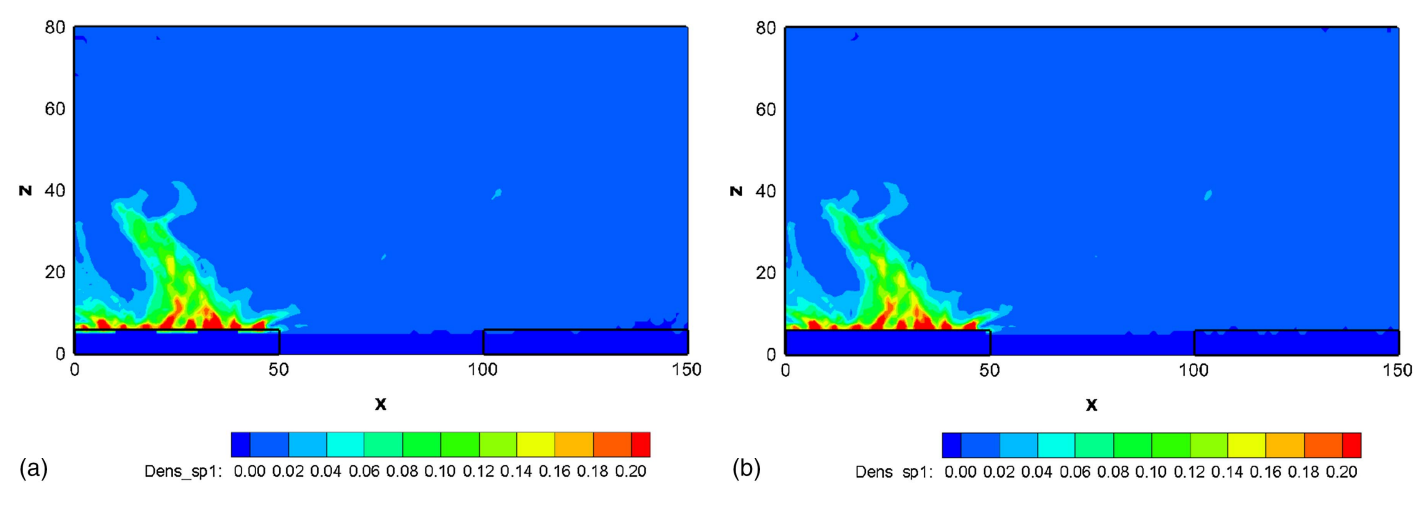


Fig. 13. Normalized dust concentration of Case 3: (a) $r_d = 1.0 \times 10^{-6}$ m; and (b) $r_d = 10.0 \times 10^{-6}$ m. Coordinates are normalized by 1.38 m.

convex surface terrain, lofted charged dust originated inside the shadow region tended to concentrate within the shadow region, whereas the charged dust originated outside the shadow region could migrate further; in addition, dust lofted on one side of the structure was not likely to reach the other side of the structure. For the concave surface terrain, dust generated inside the pit was not likely to migrate out of the pit; likewise, dust generated outside the pit was not likely to migrate into the pit. Most of the charged dust grains would concentrate near where they are originated, although a slight amount of dust could migrate further depending on amount of dust charge.

Based on these simulation results of dust concentration for a 10° Sun elevation angle (near 80° latitude at polar regions), it is recommended that future surface excavation and construction activities to be performed inside the shadow region of a convex surface structure because in such scenario, the lofted dust is likely to concentrate inside the shadow region. For necessary activities outside the shadow region, the upwind region of a surface structure should be preferred over the downwind region because the lofted dust that originated in the downwind region tended to migrate further. In addition, excavation and construction activities inside a lunar pit are expected to see localized dust clouds. Ongoing work is investigating effects of solar wind conditions and angles, 3D configurations including surface terrain and infrastructure shapes, as well as plasma—dust coupling.

Data Availability Statement

Some data, models, or code that support the findings of this study are available from the corresponding author upon reasonable request.

Acknowledgments

This work was partially supported by NASA-Missouri Space Grant Consortium through NASA-EPSCoR-Missouri, as well as NSF through Grant Nos. DMS-2111039 and CBET-2132655. The simulations presented here were performed with computing resources provided by the Center for High Performance Computing Research at Missouri University of Science and Technology through a NSF Grant (OAC-1919789).

References

Abbas, M., D. Tankosic, P. Craven, J. Spann, A. LeClair, and E. West. 2007. "Lunar dust charging by photoelectric emissions." *Planet. Space Sci.* 55 (7–8): 953–965. https://doi.org/10.1016/j.pss.2006.12.007.

Anuar, A. K. 2013. "A study of dusty plasma environment." Ph.D. thesis, Dept. of Mechanical Engineering, Lancaster Univ.

Austin, A., et al. 2020. "Robotic lunar surface operations 2." *Acta Astronaut*. 176 (Nov): 424–437. https://doi.org/10.1016/j.actaastro.2020.06.038.

Baiden, G., L. Grenier, and B. Blair. 2010. "Lunar underground mining and construction: A terrestrial vision enabling space exploration and commerce." In Proc., 48th AIAA Aerospace Sciences Meeting Including the New Horizons Forum and Aerospace Exposition, 1548. Reston, VA: AIAA.

Carroll, A., N. Hood, R. Mike, X. Wang, H. Hsu, and M. Horányi. 2020. "Laboratory measurements of initial launch velocities of electrostatically lofted dust on airless planetary bodies." *Icarus* 352 (Dec): 113972. https://doi.org/10.1016/j.icarus.2020.113972.

Christoffersen, R., and J. F. Lindsay. 2009. Lunar dust effects on spacesuit systems: Insights from the Apollo spacesuits. Rep. No. NASA/TP-2009-214786. Houston: Johnson Space Center.

Corazzari, I., et al. 2021. *History and future perspectives for the evaluation of the toxicity of celestial dust*, 46. Newcastle upon Tyne, UK: Cambridge Scholars Publishing.

Farr, B., X. Wang, J. Goree, I. Hahn, U. Israelsson, and M. Horányi. 2020. "Dust mitigation technology for lunar exploration utilizing an electron beam." *Acta Astronaut*. 177 (Dec): 405–409. https://doi.org/10.1016/j .actaastro.2020.08.003.

Fu, J. H. M. 1971. "Surface potential of a photoemitting plate." *J. Geophys. Res.* 76 (10): 2506–2509. https://doi.org/10.1029/JA076i010p02506.

Gault, D. E., E. M. Shoemaker, and H. J. Moore. 1963. Spray ejected from the lunar surface by meteoroid impact. Washington, DC: National Aeronautics and Space Administration.

Gawronska, A., et al. 2020. "Geologic context and potential EVA targets at the lunar south pole." Adv. Space Res. 66 (6): 1247–1264. https://doi .org/10.1016/j.asr.2020.05.035.

Godwin, R. 2002. Vol. 1 of Apollo 17: The NASA mission reports. Burlington, ON: Apogee Books.

Halekas, J. S., G. T. Delory, D. A. Brain, R. P. Lin, M. O. Fillingim, C. O. Lee, R. A. Mewaldt, T. J. Stubbs, W. M. Farrell, and M. K. Hudson. 2007. "Extreme lunar surface charging during solar energetic particle events." *Geophys. Res. Lett.* 34 (2): L02111. https://doi.org/10.1029/2006GL028517.

Han, D., J. Wang, and X. He. 2018. "Immersed finite element particle-incell simulations of plasma charging at the lunar terminator." *J. Space-craft Rockets* 55 (6): 1490–1497. https://doi.org/10.2514/1.A34002.

- Hartung, J. B., F. Hörz, and D. E. Gault. 1972. "Lunar microcraters and interplanetary dust." In Vol. 3 of *Proc.*, *Lunar and Planetary Science Conf.*, 2735. Houston: Lunar and Planetary Institute.
- Heiken, G. H., D. T. Vaniman, and B. M. French. 1991. Lunar sourcebook: A user's guide to the moon. Cambridge, UK: Cambridge University Press.
- Kawamoto, H. 2020. "Vibration transport of lunar regolith for in situ resource utilization using piezoelectric actuators with displacementamplifying mechanism." J. Aerosp. Eng. 33 (3): 04020014. https://doi .org/10.1061/(ASCE)AS.1943-5525.0001128.
- Lane, J. E., P. T. Metzger, and J. W. Carlson. 2010. "Lunar dust particles blown by lander engine exhaust in rarefied and compressible flow." In Proc., 12th Biennial Int. Conf. on Engineering, Construction, and Operations in Challenging Environments, 134–142. Reston, VA: ASCE.
- Lund, D., J. Zhao, A. Lamb, and D. Han. 2020. "Fully kinetic pife-pic simulations of plasma charging at lunar craters." In *Proc.*, AIAA Scitech 2020 Forum. Reston, VA: American Institute of Aeronautics and Astronautics.
- McCoy, J. E., and D. R. Criswell. 1974. Evidence for a high altitude distribution of lunar dust. Oxford: Pergamon Press.
- Metzger, P. 2005. "Rocket exhaust cratering: A serious challenge for space exploration." In *Proc.*, 11th ASCE Aerospace Division Int. Conf. (Earth and Space 2008), 2–3. Reston, VA: ASCE.
- Metzger, P. T., J. E. Lane, and C. D. Immer. 2008. "Modification of Roberts' theory for rocket exhaust plumes eroding lunar soil." Preprint, submitted April 12, 2022. http://arxiv.org/abs/2104.05198.
- Metzger, P. T., J. Smith, and J. E. Lane. 2011. "Phenomenology of soil erosion due to rocket exhaust on the moon and the Mauna kea lunar test site." J. Geophys. Res. Planets 116 (E6): E06005. https://doi.org/10.1029 /2010JE003745.
- Metzger, P. T., K. Zacny, and P. Morrison. 2020. "Thermal extraction of volatiles from lunar and asteroid regolith in axisymmetric Crank-Nicolson modeling." *J. Aerosp. Eng.* 33 (6): 04020075. https://doi. org/10.1061/(ASCE)AS.1943-5525.0001165.
- Morris, A. B., D. B. Goldstein, P. L. Varghese, and L. M. Trafton. 2016. "Lunar dust transport resulting from single- and four-engine plume impingement." AIAA J. 54 (4): 1339–1349. https://doi.org/10.2514/1.J054532.
- NASA (National Aeronautics and Space Administration). 2020. "Artemis plan." Accessed September 21, 2020. https://www.nasa.gov/sites/default/files/atoms/files/artemis_plan-20200921.pdf.
- Nitter, T., O. Havnes, and F. Melandsø. 1998. "Levitation and dynamics of charged dust in the photoelectron sheath above surfaces in space." J. Geophys. Res. Space Phys. 103 (A4): 6605–6620. https://doi.org/10 .1029/97JA03523.
- Poppe, A., J. S. Halekas, and M. Horányi. 2011. "Negative potentials above the day-side lunar surface in the terrestrial plasma sheet: Evidence of non-monotonic potentials." *Geophys. Res. Lett.* 38 (2): L02103. https:// doi.org/10.1029/2010GL046119.

- Poppe, A. R., M. Piquette, A. Likhanskii, and M. Horányi. 2012. "The effect of surface topography on the lunar photoelectron sheath and electrostatic dust transport." *Icarus* 221 (1): 135–146. https://doi.org/10.1016/j.icarus.2012.07.018.
- Rhodes, D. J., W. M. Farrell, and L. M. Jason. 2020. "Tribocharging and electrical grounding of a drill in shadowed regions of the moon." Adv. Space Res. 66 (4): 753–759. https://doi.org/10.1016/j.asr.2020.05.005.
- Sharma, H., M. Hedman, D. Wooden, A. Colaprete, and A. Cook. 2021. "Constraining low-altitude lunar dust using the LADEE-UVS data." J. Geophys. Res. Planets 126 (11): e2021JE006935.
- Wagner, S. A. 2006. The Apollo experience lessons learned for constellation lunar dust management. NASA Technical Publication TP-2006-213726. Washington, DC: National Aeronautics and Space Administration.
- Wang, J., X. He, and Y. Cao. 2008. "Modeling electrostatic levitation of dust particles on lunar surface." *IEEE Trans. Plasma Sci.* 36 (5): 2459–2466. https://doi.org/10.1109/TPS.2008.2003016.
- Wang, J., X. M. He, and Y. Cao. 2007. "Modeling spacecraft charging and charged dust particle interactions on lunar surface." In *Proc.*, 10th Spacecraft Charging Technology Conf. Houston: Lunar and Planetary Institute.
- Wang, X., J. Schwan, H.-W. Hsu, E. Grün, and M. Horányi. 2016. "Dust charging and transport on airless planetary bodies." *Geophys. Res. Lett.* 43 (12): 6103–6110. https://doi.org/10.1002/2016GL069491.
- Watkins, R. N., et al. 2021. "Understanding and mitigating plume effects during powered descents on the moon and mars." Preprint, submitted February 24, 2021. http://arxiv.org/abs/2102.12312.
- Woodcock, G. R., et al. 1990. Robotic lunar surface operations: Engineering analysis for the design, emplacement, checkout and performance of robotic lunar surface systems. NASA Contractor Report. Rep. No. NAS2-12108. Huntsville, AL: Boeing Aerospace & Electronics.
- Zhao, J., X. Wei, X. Du, X. He, and D. Han. 2021a. "Photoelectron sheath and plasma charging on the lunar surface: Semianalytic solutions and fully-kinetic particle-in-cell simulations." *IEEE Trans. Plasma Sci.* 49 (10): 3036–3050. https://doi.org/10.1109/TPS.2021.3110946.
- Zhao, J., X. Wei, X. He, D. Han, and X. Du. 2021b. "Fully-kinetic particle-in-cell simulations of photoelectron sheath on uneven lunar surface." In *Proc.*, AIAA Scitech 2021 Forum. AIAA Rep. No. 2021-1433. Reston, VA: American Institute of Aeronautics and Astronautics.
- Zhao, J., X. Wei, Z. Hu, X. He, D. Han, Z. Hu, and X. Du. 2020. "Photoelectron sheath near the lunar surface: Fully kinetic modeling and uncertainty quantification analysis." In *Proc.*, AIAA Scitech 2020 Forum. AIAA Rep. No. 2020-1548. Reston, VA: American Institute of Aeronautics and Astronautics.
- Zimmerman, M. I., W. M. Farrell, C. M. Hartzell, X. Wang, M. Horanyi, D. M. Hurley, and K. Hibbitts. 2016. "Grain-scale supercharging and breakdown on airless regoliths." *J. Geophys. Res. Planets* 121 (10): 2150–2165. https://doi.org/10.1002/2016JE005049.
- Zook, H. A., and J. E. McCoy. 1991. "Large scale lunar horizon glow and a high altitude lunar dust exosphere." *Geophys. Res. Lett.* 18 (11): 2117– 2120. https://doi.org/10.1029/91GL02235.